SLAC/AP-34
September 1984
(AP)

PARTICLE-IN-CELL SIMULATION OF HIGH POWER KLYSTRONS*

SIMON YU
Stanford Linear Accelerator Center
Stanford University, Stanford, California 94305

1. INTRODUCTION

A realistic modelling of high power Klystrons must embody certain general features:

1. The theory must be able to handle large signals. Most of the existing theories of klystrons are valid only in the small signal regime. However, these approximations fail for the penultimate and output cavities of high power klystrons.
2. Associated with the large signals are rather complex particle trajectories. The theory must be able to handle particle crossing, or in extreme cases, particles turning back. This feature automatically excludes fluid-type models.
3. The high power klystrons involve electron beams of high intensity. Self-field effects are very strong. The theory must be able to handle these effects well.
4. Particle energies are sufficiently high that a relativistic treatment of particle motion is necessary. Treatment of the field equations must similarly be relativistic.
5. Since radial dynamics play a major role in determining the efficiency of the klystron, radial resolution is an essential ingredient to any realistic modelling.

All the above features can be incorporated in a self-consistent manner in a particle-in-cell code. Our modelling of the high power klystron is based on a computer code MASK[1] constructed by Adam Drobot. This time-dependent code advances the full Maxwell's Equations together with relativistic equations of motion

---

*Work supported by the Department of Energy, contract DE-AC03-76SF00515.

for a large number of macroparticles. The major assumption made in our modelling is that of axisymmetry. Hence the fields and currents are assumed to depend on the radial coordinate r and the axial co-ordinate z. Treatment of non-axisymmetric effects would require a 3-D code.

A procedure for modelling high power klystrons using MASK has been developed. The purpose of this note is to present this procedure, and to illustrate with numerical results the practicality and validity of this procedure. Some checks on the validity of code results will also be presented. The method that we have developed is quite general and should be applicable to any high power klystron. However, for concreteness, we will confine ourselves to the modelling of the existing klystron tube XK-5 in our numerical examples. The efficiency calculated from MASK is in agreement with the data well within the statistical uncertainties of the experiments.

For all of the existing high power tubes, the pulse length is long, the transients associated with the initial turn-on happen on a relatively short time scale and the important parameter is the efficiency in steady-state. For the steady-state problem, it turns out to be possible to replace the full cavities with RF voltages across corresponding ports. This 'port approximation' leads to tremendous savings in computational efficiency and is generally well justified for the modelling of steady-state. This is a key feature in the present treatment and is described in detail in Section 2. The actual implementation of the 'port approximation' takes on different forms for the input cavity, the idler cavities immediately following the input, the penultimate cavity, and for the output cavity respectively. The methods developed for each of these cavities will be described in Section 3, and are illustrated with specific examples for the XK-5. For the numerical studies of Section 3, we assume for simplicity a constant axial magnetic field of 1 kG. Since the efficiency of the real tube is known to be sensitively dependent on the axial magnetic profile, it is not surprising that the final efficiency calculated from Section 3 deviates from the actual efficiency measured by a large amount. In Section 4, we show that by putting in the measured axial magnetic field profile, the calculated efficiency was in agreement with experimental data. In Section 5, we conclude with some general remarks regarding the potential usage of this code for the design of future klystrons.

2. PORT APPROXIMATION

As a beam enters a klystron, over an initial period of many RF cycles, the cavities are being filled until eventually, steady-state is reached. The steady-state for the cavities are in general dominated by a single mode with a relatively simple field structure. In particular, the voltage across the port is a simple oscillatory function of time. In the 'port approximation,' the cavities external to the drift tube are not modelled explicitly, but instead the effect of the cavities are modelled with equivalent RF voltages across the ports. (See Fig. 1). For a given beam, the voltages across the ports are of course not arbitrary, but are determined by the cavity characteristics. How to determine these voltages is one of the main subjects of this note.

In principle, it is not necessary to make the port approximation. We can in fact model all cavities with the actual geometries. MASK is quite capable of handling odd configurations. However, an approach like this is impractical for the following reasons:

1. In actual computer run, the klystron is modelled by a finite mesh of spatial grid points. By including the entire klystron with all cavities, the physical extent of the system is larger, and therefore, one will need to use many more spatial grid points, or, if one stays with the same number of grid points, then one will have to resort to a coarser grid. This leads in turn to a loss of resolution in the regions where we need details of beam dynamics.

2. It takes many RF cycles to fill the cavities to reach steady-state. Hence, this approach will take a very long computational time, and a code run becomes prohibitively expensive.

3. The steady-state is a resonance phenomenon. The voltage induced across the cavities is a critical function of the cold cavity properties (Q_0, ω_0, and R/Q). However, on a coarse spatial grid, it is quite difficult to get these cavity characteristics precisely, and the resulting voltages calculated could therefore be way off.

Using the port approximation, it is possible to model the entire klystron. In this simulation (see Fig. 2) the full XK-5 is modelled by a drift tube with five ports

at positions corresponding to the openings to the external cavities. At the two ends of the drift tube are two ground planes. These ground planes are introduced for convenience, but they are generally placed far from the cavities so as to minimize their effects on beam performance. For the series of calculations which we will present in Section 3. The beam was injected cold into a constant axial magnetic field of 1 kG. In this simulation, there are 512 axial grid points and 14 radial grid points. The whole run (to reach steady-state) takes about one hour of the SLAC IBM time, or approximately five minutes of CRAY time at the present. If the corresponding run were to be made with real cavities, the running time would be formidable (not to mention the fact that the final answer could be quite inaccurate).

The voltages across the ports are induced by RF components of the current. A general relation between the RF currents and the voltages could be derived by using power balance arguments.[2,3] For a given cavity, the following relations hold in general:

$$Re \int E_1 \times J_1 \, d^3r = -\frac{V_g^2}{Q_0(R/Q)} + Re\, \hat{P}_{ext} \tag{1}$$

$$Im \int E_1 \times J_1 \, d^3r = \frac{2}{(R/Q)}\left(\frac{\omega_0 - \omega}{\omega}\right) V_g^2 + Im\, \hat{P}_{ext} \tag{2}$$

In Eq. (1), the left-hand side of the equation represents work done by the fields on the beam. E_1 is the cavity-field and is proportional to the gap voltage V_g. J_1 is the first harmonic of the current density. The first term on the right-hand side represents the power loss in the cavity. The important feature here is that we do not need to know the details of the cavity geometry. We need only to know that the power loss is proportional to the square of the gap voltage V_g, the constant of proportionality is related to the **cold** cavity characteristics. For the real part of the power loss, the relevant parameters are Q_0 and R/Q. The second term on the right-hand side of Eq. (1) represents the effect of external power input/output. $\hat{P}_{ext}$ is the peak input power for the input cavity and is the negative of the peak power output for the output cavity. $\hat{P}_{ext} = 0$ for the idler cavities. Equation (2) is similarly the power balance statement for the imaginary components. The only thing to note here is that the cavity term is again proportional to V_g^2, but the constant of proportionality is related to the frequency shift $\omega_0 - \omega$, where ω_0 is

the resonant frequency of the cold cavity, while ω is the operating frequency of the tube.

Equations (1) and (2) represent a self-consistency condition which must be satisfied for every cavity. This pair of equations can be viewed as an implicit relation to determine the gap voltage V_g and the phase ϕ_g. The phase ϕg comes in through the electric field E_1. In addition the current J_1 is affected by the gap voltage and phase in some generally nonlinear way. The methods of finding the solutions of Eqs. (1) and (2) are different for each of the cavities, and will be described in greater detail in Section 3.

A rigorous derivation of Eqs. (1) and (2) will be presented in a more detailed report in the future. Here we will make the following assertions: these relations were derived from a variation of the well-known Poyntings Theorem, and is valid both for small and large signals. Although the theorem involves only the first harmonic of the current, it is correct even when large higher harmonics of the current are present. The only approximation made in deriving the theorem is that $(\omega_0 - \omega)/\omega \ll 1$. Hence, usage of this relation for all cavities is justified.

For a typical MASK run, we specify V_g and ϕ_g as inputs to the code, and compute the real and imaginary part of $\int E_1 \times J_1 \, d^3r$ as the output from the code. A straightforward evaluation of this integral is exceedingly cumbersome, since the evaluation of the first harmonic of the current density means that we have to store away the time history over one RF period of the current density at each point in space. For a typical run, this involves storing away $256 \times 512 \times 14 \times 2 \approx 3.6$ million words. Instead, we introduce the following diagnostic into our code:

$$S(t) \equiv \int \vec{e}\,(\vec{r}) \times \vec{J}\,(\vec{r}\,, t) d^3r \tag{3}$$

where $\vec{e}\,(\vec{r})$ is the electric field at the position $\vec{r}$ normalized to the field $E_g \equiv -V_g/d$ at the port. d is the gap width at the port. Since the cavity fields have the same phase everywhere, the time dependence drops out in the normalized field distribution $\vec{e}\,(\vec{r})$. S_1 and ϕ_1 are the amplitude and phase of the first harmonic of $S(t)$. The parameter S_1 is related to the induced current by

$$I_{ind} = S_1/d \quad . \tag{4}$$

All the essential information regarding beam dynamics is contained in the two parameters I_{ind} and ϕ_1, since, by straightforward algebra, we can show

$$Re \int E_1 \times J_1 \, d^3r = -V_g \, I_{ind} \cos(\phi_1 - \phi_g) \tag{5}$$

$$Im \int E_1 \times J_1 \, d^3r = -V_g \, I_{ind} \sin(\phi_1 - \phi_g) \quad . \tag{6}$$

Before we conclude this section, a point of convention needs to be clarified. The parameter (R/Q) is generally introduced via its relation to the stored energy U:

$$U = \frac{V_g^2}{(R/Q)} \quad . \tag{7}$$

In the conventional definition, the gap voltage refers to the line integral of Ez along the axis. (We call this voltage V_{axis}.) In contrast, our gap voltage V_g refers to the line integral across the port. Hence our definition of (R/Q) differs from the standard on-axis definition by

$$(R/Q) = \frac{V_g^2}{V_{axis}^2} (R/Q)_{axis} \quad . \tag{8}$$

This is an important distinction to keep in mind when we work through the numerical examples.

3. SOLUTIONS TO THE POWER BALANCE RELATIONS

In this section, we will present methods for finding the solutions to the power balance relations [Eqs. (1) and (2)]. The numerical examples are based on the grid presented in Fig. 2. A cold beam (i.e., no transverse velocities and no spread in longitudinal velocity) of 293 Amps at 270 kV, with a radius of 1 cm, is injected uniformly into the drift region. A constant axial magnetic field of 1 kG is present through the entire simulation. We will present the results for the input cavity, the two idler cavities immediately following the input gap, the penultimate cavity, and for the output cavity respectively.

3.1 INPUT CAVITY

For the input cavity, we may rewrite the power balance equation in terms of the average transmitted power P_{in} (with associated phase ϕ_{in}). We have

$$V_g I_{ind} \cos(\phi_1 - \phi_g) = \frac{V_g^2}{Q_0(R/Q)} + 2P_{in}\cos(\phi_{in} - \phi_g) \tag{9}$$

$$V_g I_{ind} \sin(\phi_1 - \phi_g) = -\frac{2}{(R/Q)}\left(\frac{\omega_0 - \omega}{\omega}\right) V_g^2 + 2P_{in}\sin(\phi_{in} - \phi_g) \tag{10}$$

For the purpose of direct comparison with experimental data, it is most useful to relate the gap voltage to the available power P_a, which is generally larger than the transmitted power P_{in} unless the matching to the external load is perfect. The general relation between the available power and the voltage is given by

$$P_a = \frac{1}{8} Q_{ext}(R/Q) I I^* \tag{11}$$

where

$$I \equiv \left[\frac{V_g}{Q_{ext}(R/Q)} - I_{ind}\cos(\phi_1 - \phi_g)\right] - i\left[\frac{2}{(R/Q)}\left(\frac{\omega_0 - \omega}{\omega}\right) V_g + I_{ind}\sin(\phi_1 - \phi_g)\right] \tag{12}$$

Note that the Q_{ext}, which includes the effects of the external load, enters Eqs. (11) and (12), in contrast to the relations for the transmitted power [Eqs. (9) and (10)] which involve Q_0, which is for the cold cavity alone.

Equations (11) and (12) may be viewed as a direct relation between the gap voltage and the available power. Hence, for a given run, we may specify the gap voltage V_g, obtain I_{ind} from the code, and compute P_a using Eqs. (11) and (12). The results for the induced current from several runs, varying V_g, are plotted in Fig. 3. The induced current is seen to be linearly proportional to gap voltage, giving rise to a quadratic relation between the power and voltage. For $Q_{ext} = 250$, on-axis R/Q of 100, and cold resonant frequency of 2860 MHz (the operating frequency being 2856 MHz), the MASK results can be summarized as

$$\frac{P_a}{50\,W} = \left(\frac{V_g}{1\,kV}\right)^2 \quad . \tag{13}$$

The phase is constant for all runs, with

$$\phi_1 - \phi_g = -3.0 \,\text{radians} \quad . \tag{14}$$

These code results are independent of the gap phase ϕ_g, as we would expect from time translational invariance of the system. The value of -3.0 for $\phi_1 - \phi_g$ is initially somewhat surprising since one would expect from small signal theory for narrow gaps a value close to $-\pi/2$. In the Appendix, we present an analysis to show that the phase change computed by the code is indeed reasonable.

3.2 Idler Cavities — Small Signal

We next consider the second and third cavities of an XK-5. Both of these are idler cavities, and lie generally in the regime where small signal theories are valid. In the idler cavities, there are no external power input/output, and the power balance relation becomes

$$V_g \, I_{ind} \cos(\phi_1 - \phi_g) = \frac{V_g^2}{Q_0 (R/Q)} \tag{15}$$

$$V_g \, I_{ind} \sin(\phi_1 - \phi_g) = -\frac{2}{(R/Q)} \left(\frac{\omega_0 - \omega}{\omega} \right) V_g^2 \tag{16}$$

Taking the ratio of Eqs. (15) and (16), we obtain a relation for the phase

$$\phi_1 - \phi_g = \tan^{-1} \left[-2 Q_0 \left(\frac{\omega_0 - \omega}{\omega} \right) \right] \equiv \Psi \tag{17}$$

From the sum of the square of Eqs. (15) and (16), we obtain a ratio between the induced current and the gap voltage

$$\frac{I_{ind}}{V_g} = \frac{1}{(R/Q)} \left[\left(\frac{1}{Q_0} \right)^2 + \left\{ \frac{2(\omega_0 - \omega)}{\omega} \right\}^2 \right]^{\frac{1}{2}} \equiv \alpha \tag{18}$$

Note that on the right-hand side of Eqs. (17) and (18), we have expressions which are related only to cold cavity properties, and nothing else. Hence the two parameters Ψ and α are fixed once the cavity characteristics are specified. For the second and third cavities of the XK-5, these parameters are determined to be $\Psi^{(2)} = -1.49 \quad \alpha^{(2)} = 9.3 \times 10^{-5}$, and $\Psi^{(3)} = -1.52 \quad \alpha^{(3)} = 1.44 \times 10^{-4}$. All quantities are expressed

in MKS units and the difference in convention for R/Q, as described in Section 2, has been taken into account.

Equations (17) and (18) may now be viewed as a pair of impedance relations, requiring that the phase difference between the induced current and the gap voltage, and the ratio of the magnitudes be fixed by cold cavity properties. These relations are true for all idler cavities, independent of whether the signals are large or small. As we shall see, the output cavity is similarly described by a slight variation of these formulae.

To find the solution to Eqs. (17) and (18), the simplest method that comes to mind is one of straightforward iteration, i.e., assuming that we have performed the $(n-1)$ iteration to obtain the induced current $I_{ind(n-1)}$ and phase $\phi_{1(n-1)}$, the next guess for the voltage and phase is determined by

$$\phi_{g(n)} = \phi_{1(n-1)} - \Psi \tag{19}$$

$$V_{g(n)} = \frac{I_{ind(n-1)}}{\alpha} \tag{20}$$

The strategy would then be to iterate until convergence is reached.

This method does not work for the second cavity, as is evident from the results of several iterations, listed in Table 1, and plotted on Fig. 4. It is clear that convergence is nowhere in sight.

To find the solution to the impedance relations, we need to input additional physics. For the second and third cavities, the fact that the signals are small allows us to decompose the induced current into two components:

$$\vec{I}_{ind} \equiv \vec{I}_{inp} + \vec{I}_{bl} \tag{21}$$

The input current $\vec{I}_{inp}$ is the result of the bunching process occurring prior to arrival at the cavity in question. For the second cavity, we can obtain $\vec{I}_{inp}^{(2)}$ by running MASK with a finite gap voltage in the input gap, but setting $V_g^{(2)} = 0$.

$\vec{I}_{bl}$ represents the effects of beam loading, and is a direct result of the voltage induced across the same cavity. In the small signal regime, the beam loaded current

is linearly proportional to the gap voltage. Furthermore, this beam loaded current is the same as what we would calculate if the beam that enters the cavity has no RF component. The situation then becomes analogous to the input gap (which has an incoming dc beam). We can therefore employ similar time-translational invariance arguments to the beam loaded component of the current. Linearity and time-translational invariance in the small signal regime allow us to write

$$I_{bl} = V_g \, \bar{I}_{bl} \tag{22}$$

$$\phi_{bl} = \phi_g + \bar{\phi}_{bl} \tag{23}$$

where $\bar{I}_{bl}$ and $\bar{\phi}_{bl}$ are two constants derivable from a single MASK run with a dc beam.

The decomposition of current [Eq. (21)], and the linearity and time-translational invariance of the beam loaded current [Eqs. (22) and (23)] is well borne out by MASK results. We take the somewhat confusing results from the six runs tabulated in Table 1, and compute I_{bl} and ϕ_{bl} using Eq. (21), (with I_{inp} and ϕ_{inp} given by Run 1). The net results are plotted in Figs. 5 and 6, and are clearly consistent with Eqs. (22) and (23).

At this point, the cavity beam dynamics is described by six equations. In addition to the original two impedance relations [Eqs. (17) and (18)], we have two equations for the additivity of currents [the cosine and sine components of Eq. (21)], and two equations for linearity and time translational invariance for the beam loaded component of the current. There are six unknowns: V_g, ϕ_g, I_{ind}, ϕ_1, I_{bl} and ϕ_{bl}. Four constants in these equations (I_{inp}, ϕ_{inp}, $\bar{I}_{bl}$, $\bar{\phi}_{bl}$) are derivable from MASK runs. After some algebra, these six equations can be combined to give an explicit solution for V_g and ϕ_g

$$\phi_g = \tan^{-1}\left[\frac{I_s(\alpha_c - \beta_c) - I_c(\alpha_s - \beta_s)}{I_c(\alpha_c - \beta_c) + I_s(\alpha_s - \beta_s)}\right] \tag{24}$$

$$V_g = \frac{I_{inp}}{\left[(\alpha_c - \beta_c)^2 + (\alpha_s - \beta_s)^2\right]^{1/2}} \tag{25}$$

where we have

$$I_c = I_{inp} \cos \phi_{inp} \tag{26}$$

$$I_s = I_{inp} \sin \phi_{inp} \tag{27}$$

$$\alpha_c = \alpha \cos \Psi \tag{28}$$

$$\alpha_s = \alpha \sin \Psi \tag{29}$$

$$\beta_c = \bar{I}_{bl} \cos \bar{\phi}_{bl} \tag{30}$$

$$\beta_s = \bar{I}_{bl} \sin \bar{\phi}_{bl} \tag{31}$$

The validity of our small signal assumptions can be verified by checking the final results against the desired impedance relations. Continuing on with our example, we derive from MASK runs the input values of $S_{inp}^{(2)} = 1.24$, $\phi_{inp}^{(2)} = -0.84$, $\bar{I}_{bl}^{(2)} = 1.11 \times 10^{-4}$, and $\bar{\phi}_{bl} = -3.0$. The gap voltage and phase for the second gap were determined from Eqs. (24) and (25) to be

$$V_g^{(2)} = 8.8 \times 10^3 \, V$$

$$\phi_g^{(2)} = -0.26$$

The resulting I_{ind} and ϕ_1 gives

$$\phi_1^{(2)} - \phi^{(2)}g = -1.48$$

$$\frac{I_{ind}^{(2)}}{V_g^{(2)}} = 9.3 \times 10^{-5}$$

in excellent agreement with the desired impedance relation. The same method was used to determine the voltage and phase of the third cavity as

$$V_g^{(3)} = 5.9 \times 10^4 \, V$$

$$\phi_g^{(3)} = 0.67$$

which gives rise to an induced current of

$$\phi_1^{(3)} - \phi_g^{(3)} = -1.54$$

$$\frac{I_{ind}^{(3)}}{V_g^{(3)}} = 1.44 \times 10^{-4}$$

again in excellent agreement with the desired impedance relation for the third cavity.

3.3 The Penultimate Cavity

The small signal procedure developed so far is not expected to be valid for the fourth (penultimate) cavity, where the RF currents are quite large. However, beam loading effects are generally quite small in the penultimate cavity, making it relatively easy to achieve convergence. The reason is that the penultimate cavity is generally designed with a large detuning. For example, the fourth cavity of an XK-5 is detuned by 84 MHz. This means that for a given input current, the induced voltage is relatively small. This in turn implies that the beam loaded current would be small compared to the input current. Hence $I_{ind}^{(4)} \approx I_{inp}^{(4)}$. Following on with our numerical examples, the input current is 171 A with a phase $\phi_{inp} = -2.73$. After one iteration, we achieved convergence with $I_{ind} = 169$ A and $\phi_1 = -2.89$. With the final gap parameters of $V_g^{(4)} = 1.99 \times 10^5$ V, and $\phi_g^{(4)} = -1.33$, MASK calculated $\phi_1^{(4)} - \phi_g^{(4)} = -1.56$, and $I_{ind}^{(4)}/V_g^{(4)} = 8.5 \times 10^{-4}$. The deviation from the desired values from impedance relations is less than 2% ($\Psi^{(4)} = -1.56$, and $\alpha^{(4)} = 8.65 \times 10^{-4}$).

3.4 Output Cavity

The output cavity differs in principle from the idler cavities since in the power balance equation, there is an additional term corresponding to power output. Here, we take advantage of the fact that the output power is proportional to the wall loss

$$P_{out} = \beta P_{wall} \tag{32}$$

where the constant of proportionality β is determined by the geometry of the last cavity. The outpower is generally in phase with the field, and the contribution of the external power term to the imaginary component of the power balance equation

can therefore be set equal to zero. Hence, Eq. (10) remains identical to the idler cavities, while in Eq. (9), we have

$$\begin{aligned} P_{wall} + P_{out} &= (1+\beta)P_{wall} \\ &= \left(\frac{1+\beta}{Q_0}\right)\frac{V_g^2}{(R/Q)} \\ &= \frac{1}{Q_L}\frac{V_g^2}{(R/Q)} \end{aligned} \tag{33}$$

Hence, the output cavity is now identical in form to the idler cavities and is described by the impedance relations Eqs. (17) and (18), except that the cold cavity Q_0 is replaced by the loaded Q_L.

For the output cavity, small signal clearly does not work, and beam loading effects are dominant. However, the physics of the output gap is quite different from the idler gaps. For example, the gap voltage in the output gap is nearly in phase with the current, in contrast to the idler gaps where the gap voltage is nearly 90° out of phase with the current. This difference in physics is undoubtedly responsible for the difference in the observed convergence characteristics for the fifth cavity. What we find here is that with the straightforward iteration procedure the phases change relatively slowly from iteration to iteration, and the amplitude does converge, although the convergence is not very rapid.

An additional observation is taken advantage of to speed up convergence. As long as the choice of loaded Q_L is reasonable, the output power is a slowly varying function of the voltage $V_g^{(5)}$, as is shown in Fig. 7. An iteration scheme based on the near variance of P_{out} is developed. We assume

$$\frac{I_{ind(n)}}{V_{g(n)}} = \alpha \tag{34}$$

$$V_{g(n)}\, I_{ind(n)} = V_{g(n-1)}\, I_{ind(n-1)} \tag{35}$$

to determine the gap voltage for the nth iteration as

$$V_{g(n)} = \left[\frac{V_{g(n-1)}\, I_{ind(n-1)}}{\alpha}\right]^{1/2} \tag{36}$$

Convergence is generally achieved in two to three iterations.

3.5 SUMMARY

We have worked through one specific example of taking an electron beam through all five cavities. The final results for the gap voltage and phase for all five cavities, together with (I_{ind}/V_g) and $\phi_1 - \phi_g$ obtained are tabulated in Table 2. The desired values for α and Ψ are placed alongside the computed values for comparison. We see that the agreements between computed values and the desired values are in the 1 to 2% range.

The procedure for reaching the proper impedance relations for all cavities is summarized in Table 3. We expect typically to reach convergence in seven to eight code runs.

4. EFFECTS OF VARIABLE AXIAL MAGNETIC FIELDS

The emphasis of this note is on the **procedure** for the modelling of high power klystrons. We hope at this point to have demonstrated to the reader a method of calculation which is quite general and is workable in practice. For a realistic modelling of existing klystrons, several additional features need to be investigated:

1. Effects of variable magnetic fields. The example presented in Section 3 was performed for a non-rotating beam immersed in a constant axial magnetic field. However, for a realistic klystron, the efficiency is known to be very sensitive to the magnetic field profile. In fact the magnetic field is empirically varied to maximize the efficiency.

2. Dependence on injection conditions. The electron beam in a klystron is injected from a gun which is not modelled in the present calculations. Presumably, effects of the gun can be taken into account by injecting the beam into our simulation with particle trajectories from some other programs, such as Herrmannsfeldt's GUN program. This is a straightforward exercise, but has not yet been done.

3. The cavity parameters have some inherent uncertainties. Checks on the sensitivity of code results to these uncertainties need to be performed.

Of the three factors listed above, the effect on the klystron performance from

the variable magnetic field is probably the greatest. To incorporate this effect, we have taken the **measured** axial magnetic field profile for the XK-5 (Fig. 8), which is empirically obtained by maximizing the efficiency of the klystron, and built it into the code. The results from this case are compared to the constant Bz case.

The spatial distribution of electrons for the two cases are shown in Figs. 9 and 10. In these figures, we have displayed several snapshots of the distributions during an RF cycle after the beam has reached steady-state. The strong bunching of particles around the penultimate and output cavities is evident in both cases. However, it is clear that the radial dynamics is drastically altered by the presence of the variable magnetic field. In the latter case, Bz is quite low at entrance (< 100 G). The field increases rapidly as the beam passes the first three cavities. The angular momentum of the beam increases correspondingly due to the radial magnetic field associated with the varying Bz. The resulting $J_\theta \times Bz$ force causes a strong pinching of the beam around the location of the third cavity. The beam goes through some sausaging between the third and fourth cavity. Beyond the fourth cavity, the axial magnetic field rapidly decreases. The pinch force on the beam is then decreased, and the beam "opens up" on its way to the output cavity. The beam barely clears the output gap, and hits the wall after the output gap (in the real klystron, the collector side of the output gap is in fact enlarged somewhat to mitigate an otherwise serious problem of edge erosion). It is generally known that maximum efficiency is achieved by allowing a beam to pass the output gap as close as possible to the wall without hitting it. This feature is borne out by the code results. With the variable magnetic field, the code calculates an efficiency of 45%, which is in good agreement with the experimental data. In contrast the constant magnetic field case yields an efficiency of 34%. Loss of particles due to the beam scraping the klystron wall, as is evident in Fig. 1, is chiefly responsible for this rather low efficiency in the constant Bz case. In the run with variable Bz, the radial dimension of the tube was increased to correspond to the output end of the actual XK-5 tube. A run with the same tube dimensions, but with a constant Bz of 1 kG, yields an efficiency somewhere between 34% and 45%.

5. CONCLUSION

The purpose of this paper is two-fold:

1. To show that we have a workable tool for simulating high-power klystrons.
2. To show that results from the simulation are in reasonable agreement with "the real world."

We are reasonably confident in the validity of the procedure developed, although the actual results must be viewed as preliminary at this point. Many more sensitivity checks must be performed (and are in the process of being performed) to ascertain uncertainties in both theory and experiment.

However, it should be clear at this point that the code is able to give us a great number of details regarding the dynamics of the beam within the klystron. We list below some examples of useful information that the code is capable of giving:

(a) Effects of magnetic field on beam profile

(b) Wall-scraping effects

(c) Distribution of electrons as they hit the collector

(d) Possibilities of particles turning back, and the ultimate fate of these particles (if they move back far enough to re-enter earlier cavities, it may be a disaster)

(e) Electric field strengths at the walls for breakdown studies

(f) The code has the capability of calculating effects of "lossy" tube walls, although that capability has not been "turned on" as yet.

A code like this can clearly be exercised to check the effects on efficiency due to injection conditions, locations and parameters of the cavities, and the geometry of the tube. Given sufficient CRAY time, it is realistic to consider employing MASK as a design code.

APPENDIX

The code result for the input gap gives $\phi_1 - \phi_g = -3.0$ radians. This result seems at first sight to contradict conventional wisdom which says that for narrow

gaps the RF current should be approximately $\pi/2$ out of phase with the voltage. Allowing for the effects of a finite gap, small signal theories predict[4]

$$\phi_1 - \phi_g = -\frac{\pi}{2} - \frac{\theta}{2}$$

where the transit angle is given by

$$\theta = \frac{\omega d}{v_0}$$

with ω the driving frequency, d the gap width, and v_0 the unperturbed velocity of the beam. For the input gap with a width at port of ~ 7 mm, the phase difference, by this formula, should be –1.85. Now it is known that the electric field broadens as we move towards the center of the tube. The *Ez* profile at several radial positions, as computed by the code, is plotted on Fig. 11. The fields away from the tube edge have in general exponential tails. If we use the full-width-at-half-max as the effective gap width, we predict –2.1 radians at beam edge and –2.4 radian on beam axis. Since the beam is more or less uniform, we would expect an answer somewhere between these two values, which would be way short of the code result.

One may suspect at this point that the code is giving the wrong answer. Indeed, if one goes through the derivation of the analytic formula, one observes that the phase difference of $-(\pi/2)$ comes in a rather subtle way. Writing the RF current as

$$J_1 = \rho_0 v_1 + \rho_1 v_0 \quad ,$$

each one of the terms on the right-hand side has a phase of $-\pi$ to leading order. However, the leading terms cancel, giving as a first non-zero contribution the second order term which is proportional to $-\pi/2$. Hence, if the current laydown scheme in MASK does not recognize this detailed cancellation, it may give a number close to $-\pi$ (as the code result of -3.0 radian might suggest).

The small signal formula was rigorously derived, assuming gridded gap. In order to check the validity of the code, we constructed a special version of the code with the particle push and current laydown schemes unchanged, but with externally specified fields for a gridded gap. The code result for the gridded gap case was $\phi_1 - \phi_g = -1.9$, in good agreement with the small signal theory.

This leads us to conjecture that the large difference in phase comes from the exponential tail. We were able to confirm this by doing two analytic examples: a gridded gap, and an exponential gap (the spatial configuration of Ez falls off exponentially on both sides of gap center). For the gridded gap, the phase of the current at the center of the gap was predicted to be $-(\pi/2)-(\theta/3)$, while in the exponential case (with the same gap width), the phase was predicted to be $-(\pi/2)-\theta$. In fact, one can calculate analytically the phase of the current as a function of the axial position. In the gridded gap case, the phase is predicted to change linearly with z with a slope of $-(2/3)(\omega/v_0)$. but the exponential gap has a characteristic stationary phase of $[-(\pi/2)-\theta]$ independent of z at positions before the gap center. The phases from the analytic calculations are plotted on Fig. 12. As a check on the code, we constructed special versions with the same field profiles, and the corresponding results for the phases of the current are plotted alongside. One sees a close agreement (there is a systematic deviation in the code results due to inaccuracies in the harmonic analysis of the currents introduced in this highly specialized version of the code).

ACKNOWLEDGEMENTS

This note summarizes ideas and contributions from many individuals. I am indebted to Bill Herrmannsfeldt, Harold Hanerfeld, Adam Drobot, Perry Wilson, Marvin Chodorow, Bernie Lippmann, Dale Nielsen, and Scott Brandon for their contributions to various aspects of this problem.

REFERENCES

1. Palevsky, A., and Drobot, A. T., "Application of E-M P.I.C. Codes to Microwave Devices." Proceedings of the Ninth Conference on Numerical Simulation of Plasmas, Evanston, Illinois, 1980.
2. Johnson, C. C., "Field and Wave Electrodynamics," McGraw-Hill, 1965.
3. Collin, R., "Foundations for Microwave Engineering," McGraw-Hill, 1966.
4. Chodorow, M., and Susskind, C., "Fundamentals of Microwave Electronics," McGraw-Hill.

Table 1
Second Cavity — MASK Results
(straightforward iteration)

Run	V_g (kV)	ϕ_g	I_{ind} (A)	ϕ_1
1	0	0	1.24	−0.84
2	13.3	0.65	1.98	−1.67
3	20.9	−0.18	1.70	−2.63
4	18.0	−1.14	0.79	1.89
5	8.5	−2.90	1.79	−0.32
6	19.3	1.17	3.00	−1.48

Table 2

Summary of Results from MASK Runs

Cavity	V_g (kV)	ϕ_g	I_{ind}/V_g (A)	$\phi_1 - \phi_g$
1	1	0	1.0×10^{-4}	−3.00
2	8.79	−0.26	9.3×10^{-5} (9.3×10^{-5})*	−1.48 (−1.49)*
3	58.8	0.67	1.44×10^{-4} (1.44×10^{-4})	−1.54 (−1.52)
4	199	−1.33	8.49×10^{-4} $(8.65 \times 10^{-4}$	−1.56 (−1.56)
5	248	0.86	8.90×10^{-4} (8.81×10^{-4})	−0.12 (−0.09)

*Brackets denote target values (impedance relation).

Table 3

Summary of Procedure

Run	Mode	Products	
1	$V_g^{(1)} \neq 0$	$I_{inp}^{(2)}$	$\phi_{inp}^{(2)}$
2	$V_g^{(2)} \neq 0$	$I_{ind}^{(2)}\,\phi_{ind}^{(2)}$	$I_{inp}^{(3)}\,\phi_{inp}^{(3)}$
3	$V_g^{(3)} \neq 0$	$I_{ind}^{(3)}\,\phi_{ind}^{(3)}$	$I_{inp}^{(4)}\,\phi_{inp}^{(4)}$
4 5	$V_g^{(4)} \neq 0$	$I_{ind}^{(4)}\,\phi_{ind}^{(4)}$	$I_{inp}^{(5)}\,\phi_{inp}^{(5)}$
6 7 8(?)	$V_g^{(5)} \neq 0$	$I_{ind}^{(5)}$	$\phi_{ind}^{(5)}$

Figure Captions

1. In the "port approximation," the cavity structure (a) is replaced by a single port (b).
2. Spatial Grid for a full klystron run. The numbers on the side and top are grid indices. Positions of ports are marked on upper edge.
3. The scaled induced current $S_1 = I_{ind}\, d$ is plotted as a function of the gap voltage V_g for the input cavity of an XK-5.
4. Results of Table 1 are plotted on a polar plot. The triangles labelled 1 to 5 correspond to Runs 2 to 6 of Table 1, respectively. The lengths of the vectors are proportional to $\alpha \equiv I_{ind}/V_g$, whereas the polar angle is $\Psi \equiv \phi_1 - \phi_g$. The target values of α and Ψ, as dictated by the impedance relation, are marked by a cross circumscribed with a circle.
5. The beam-loaded current I_{bl} as computed from Eq. (22), using the data of Table 1, is plotted as a function of V_g.
6. The phase ϕ_{bl} of the beam-loaded current as computed from Eq. (23), using the data of Table 1, is plotted as a function of ϕ_g.
7. The output power as computed by MASK is shown as a function of the gap voltage for the output cavity $V_g^{(5)}$.
8. Axial magnetic field profile for the XK-5.
9. Spatial distribution of electrons. The axial magnetic field is constant (1 kG). The different pictures correspond to different phases, Φ throughout an RF cycle. Positions of the five ports are marked on top.
10. Spatial electron distribution with the axial magnetic field profile shown in Figure 8.
11. The Ez profile at the input gap at several radial positions. The axial distance ϕz is in units of grid size ($\Delta z = 0.001$ m).
12. The phase of the RF current with distance for analytic field shapes — gridded and exponential fall-off. The solid lines correspond to analytic calculations while the triangles and dots are outputs from MASK.

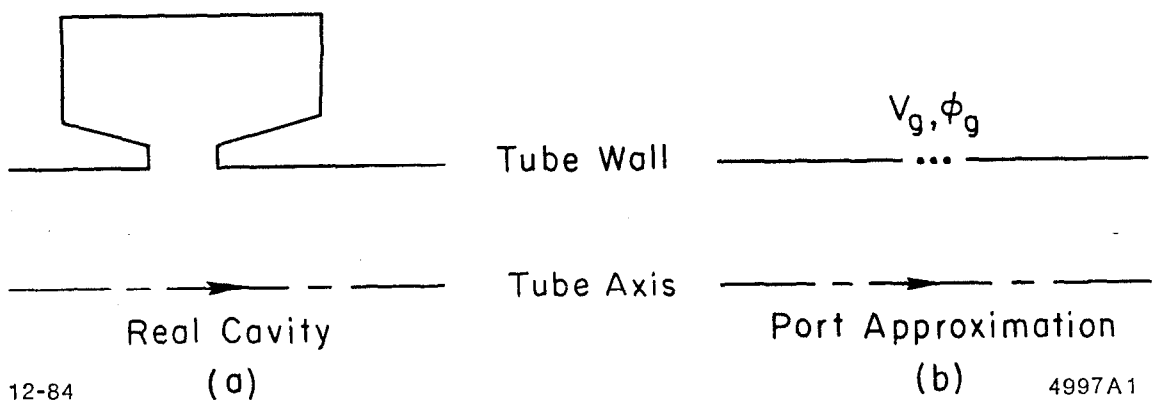
V_g, ϕ_g
Tube Wall
Tube Axis
Real Cavity
(a)
Port Approximation
(b)
12-84
4997A1

Fig. 1

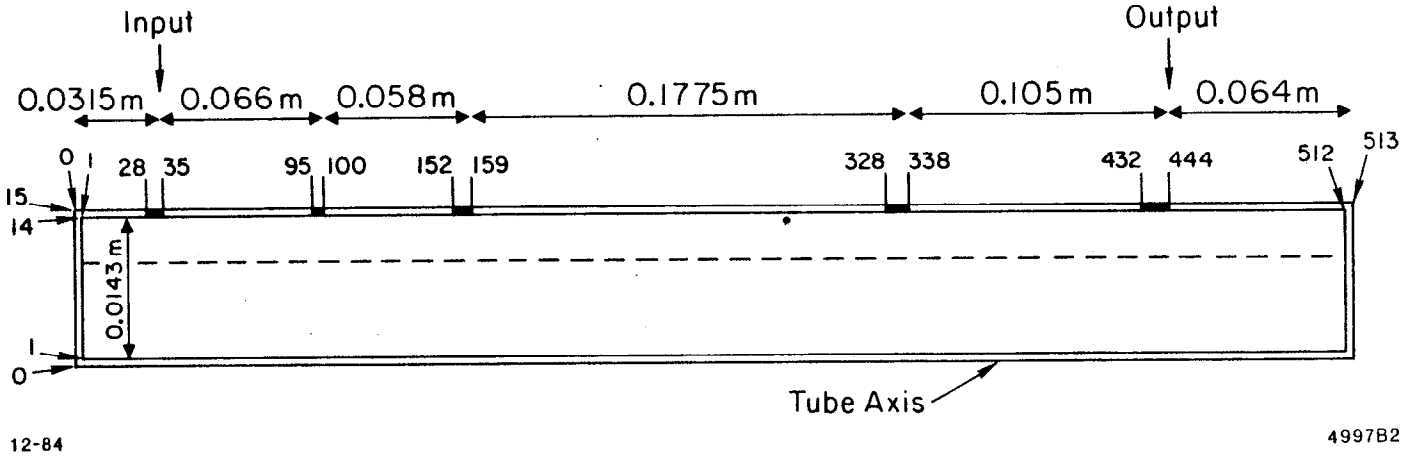
Input
Output
0.0315m
0.066m
0.058m
0.1775m
0.105m
0.064m
0
1
28
35
95
100
152
159
328
338
432
444
512
513
15
14
0.0143m
1
0
Tube Axis
12-84
4997B2

Fig. 2

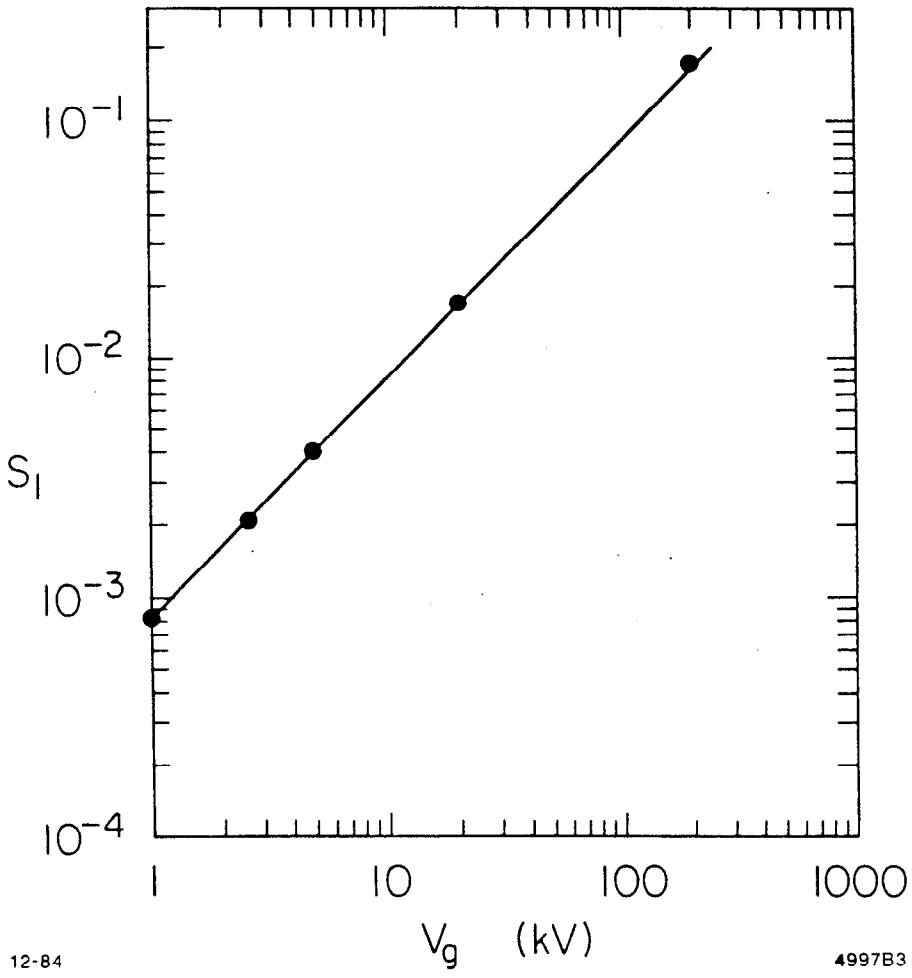

Fig. 3

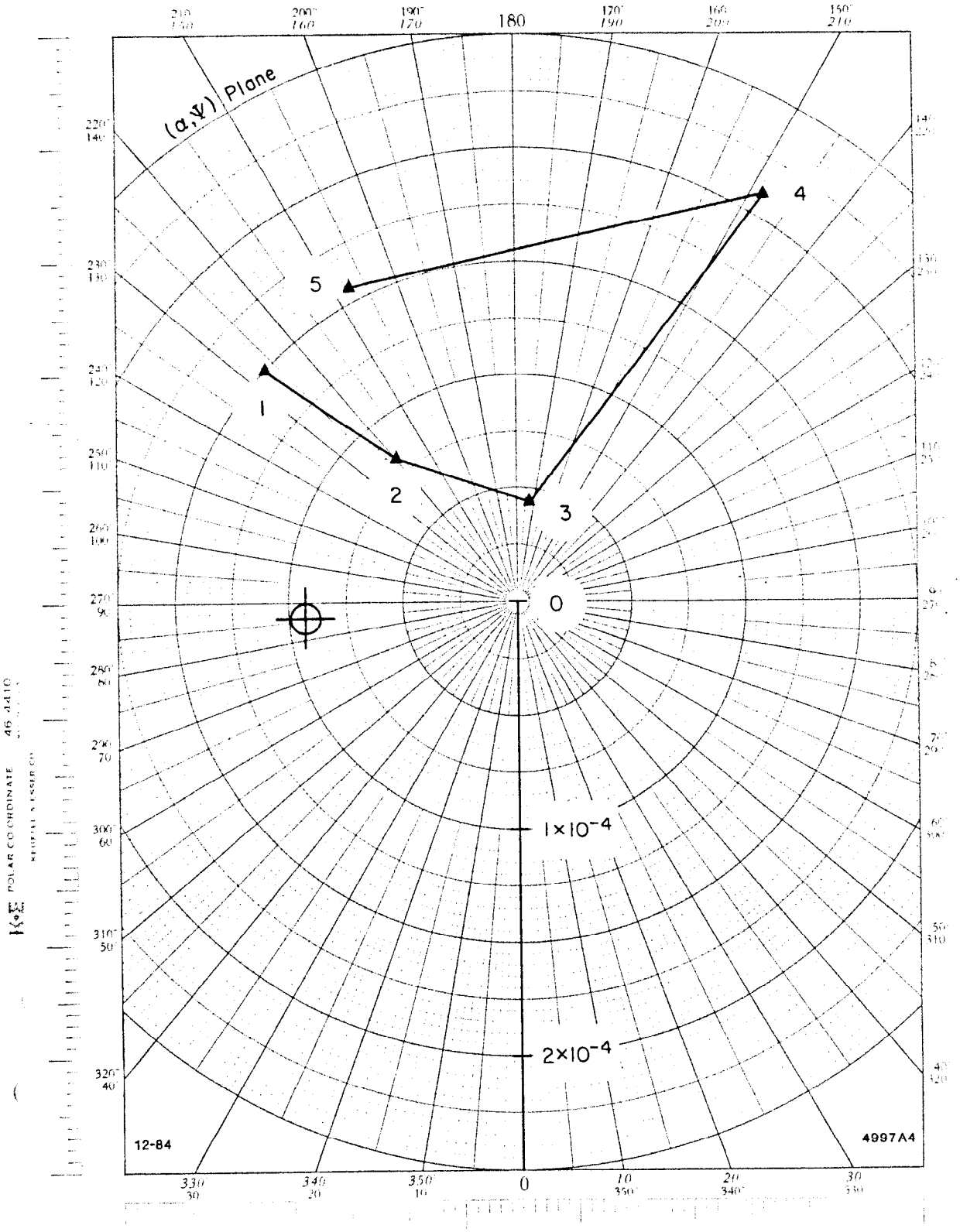

Fig. 4

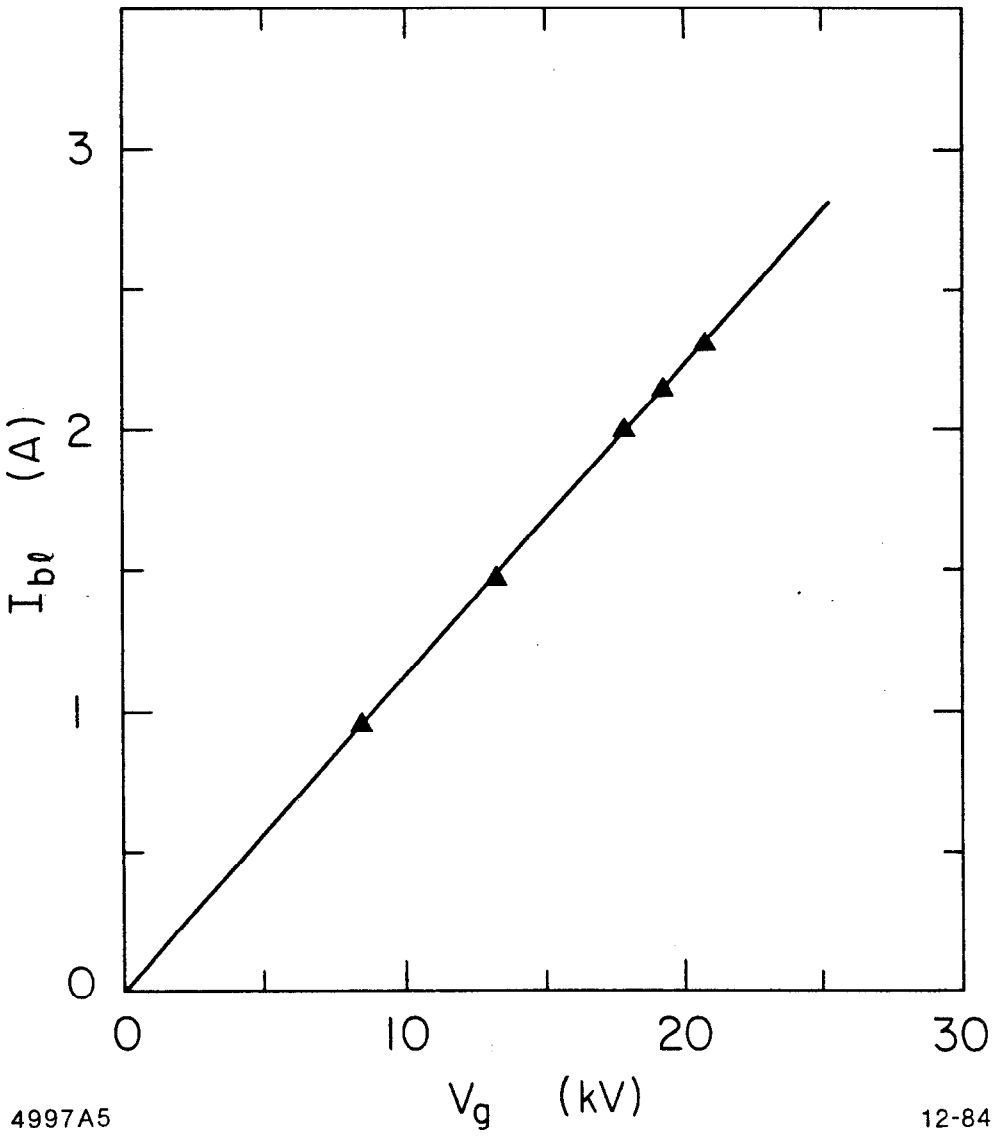

Fig. 5

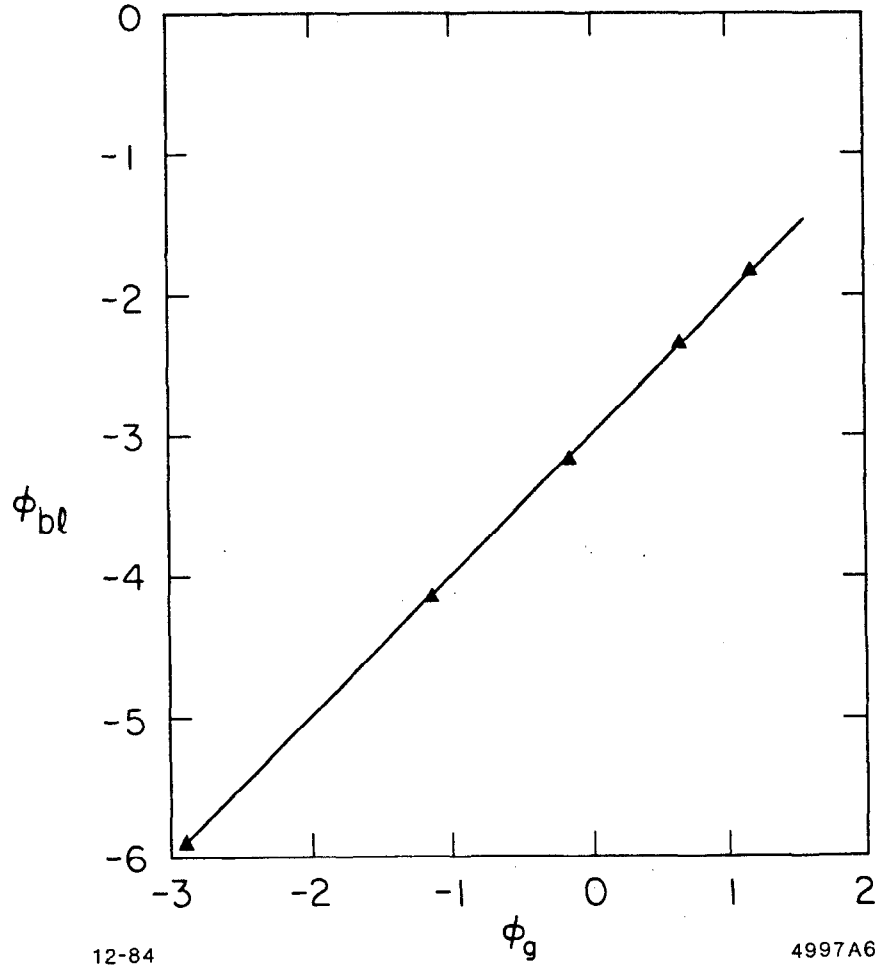

Fig. 6

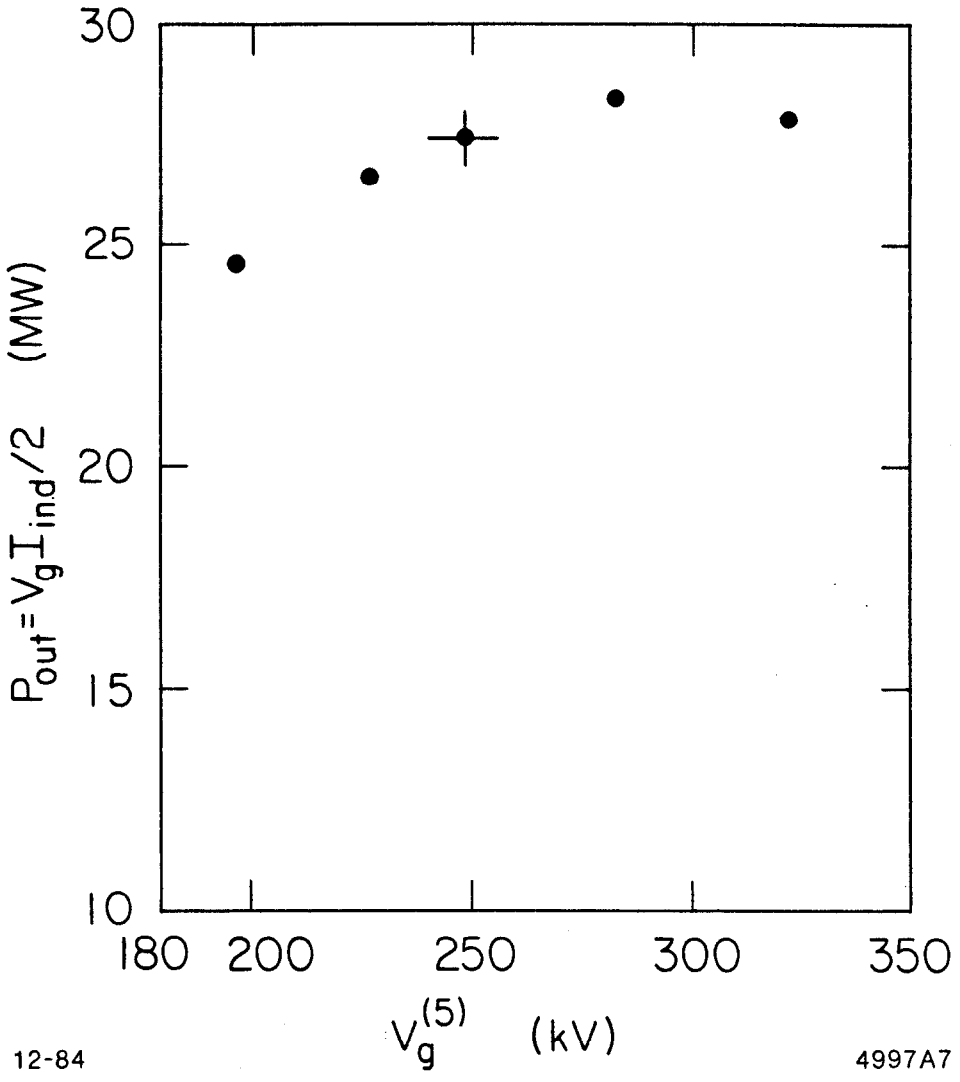
30
25
20
15
10
180
200
250
300
350
$P_{out} = V_g I_{ind}/2$ (MW)
$V_g^{(5)}$ (kV)
12-84
4997A7

Fig. 7

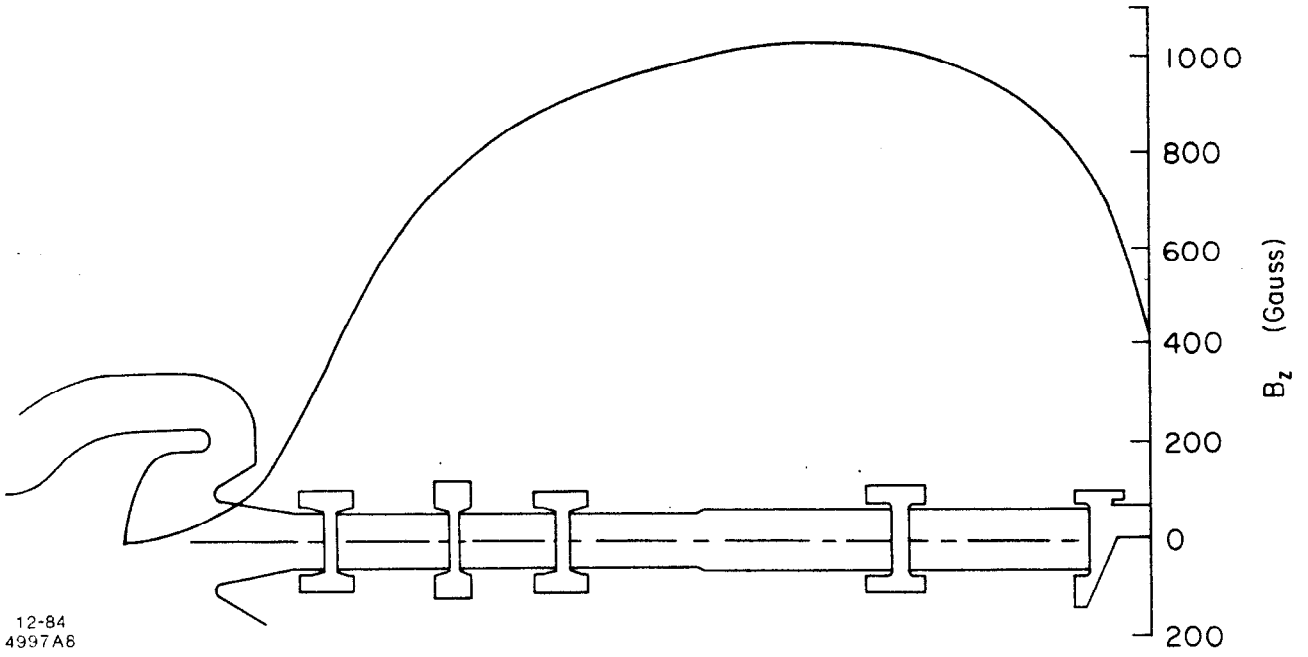

Fig. 8

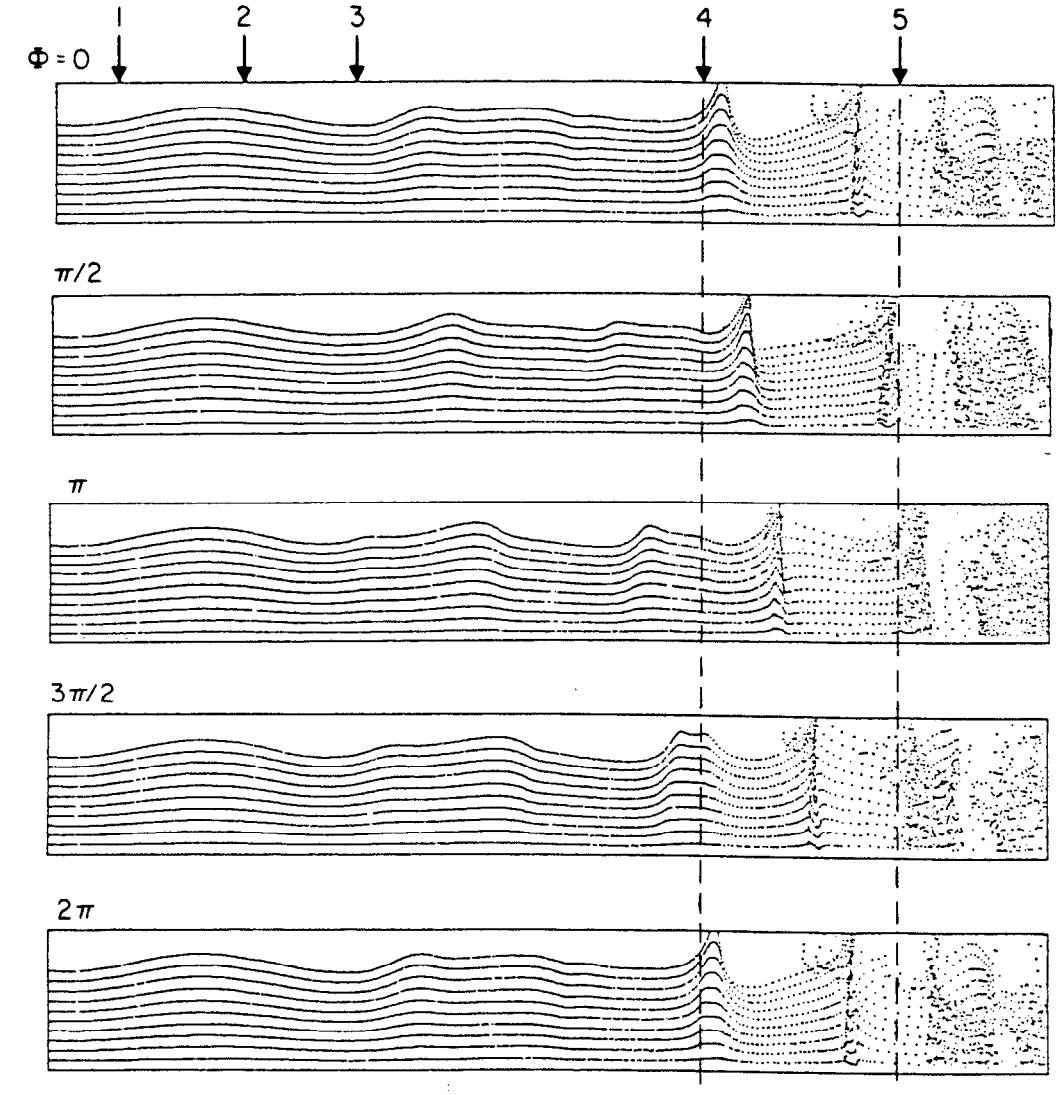

Fig. 9

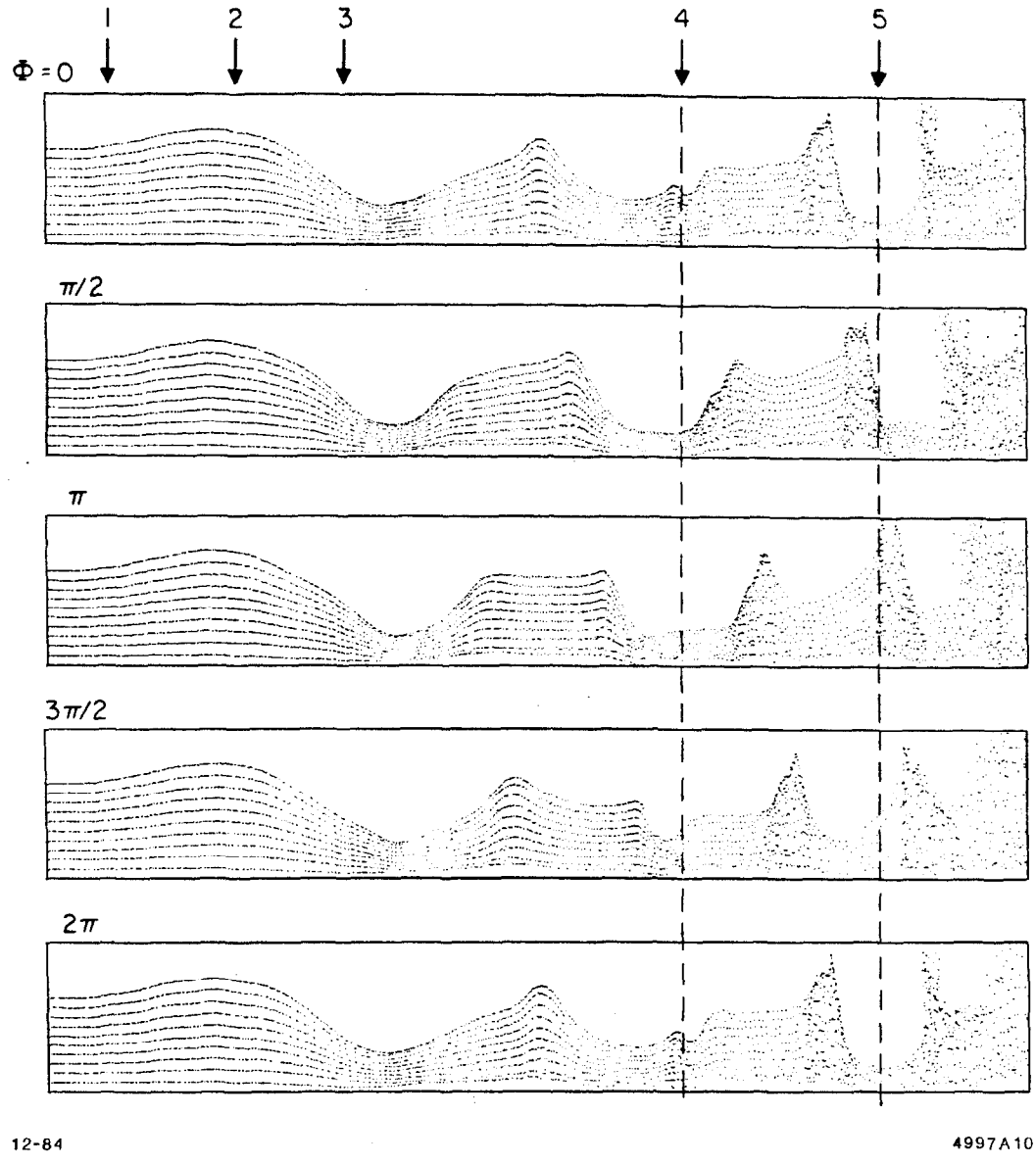

Fig. 10

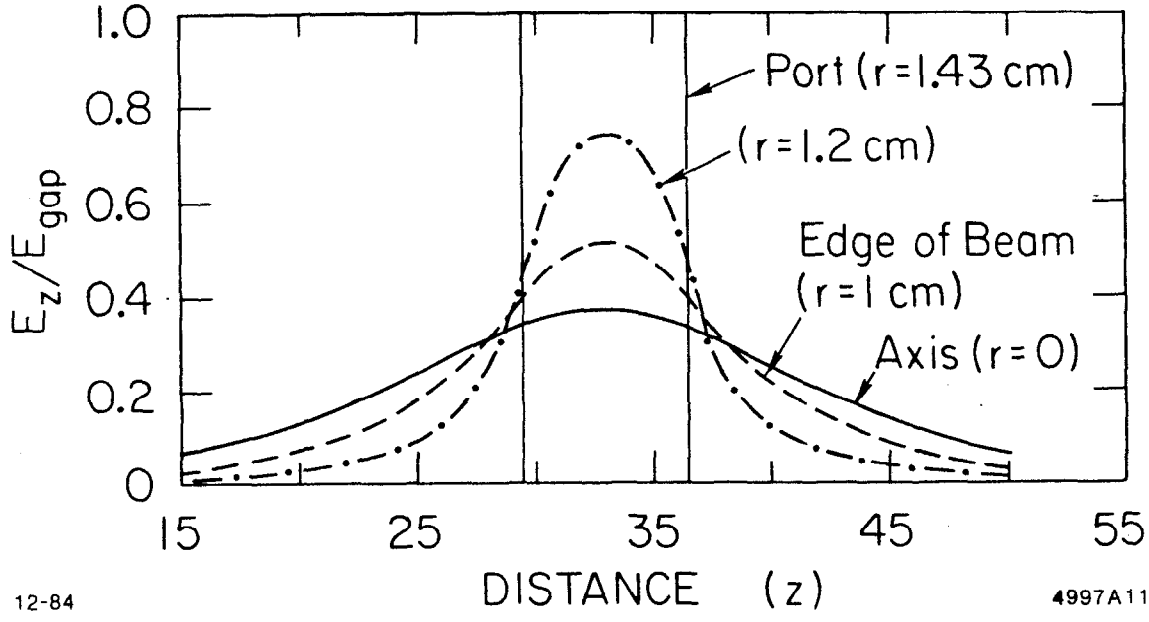
1.0
0.8
0.6
0.4
0.2
0
E_z/E_{gap}
Port (r=1.43 cm)
(r=1.2 cm)
Edge of Beam
(r=1 cm)
Axis (r=0)
15
25
35
45
55
DISTANCE (z)
12-84
4997A11

Fig. 11

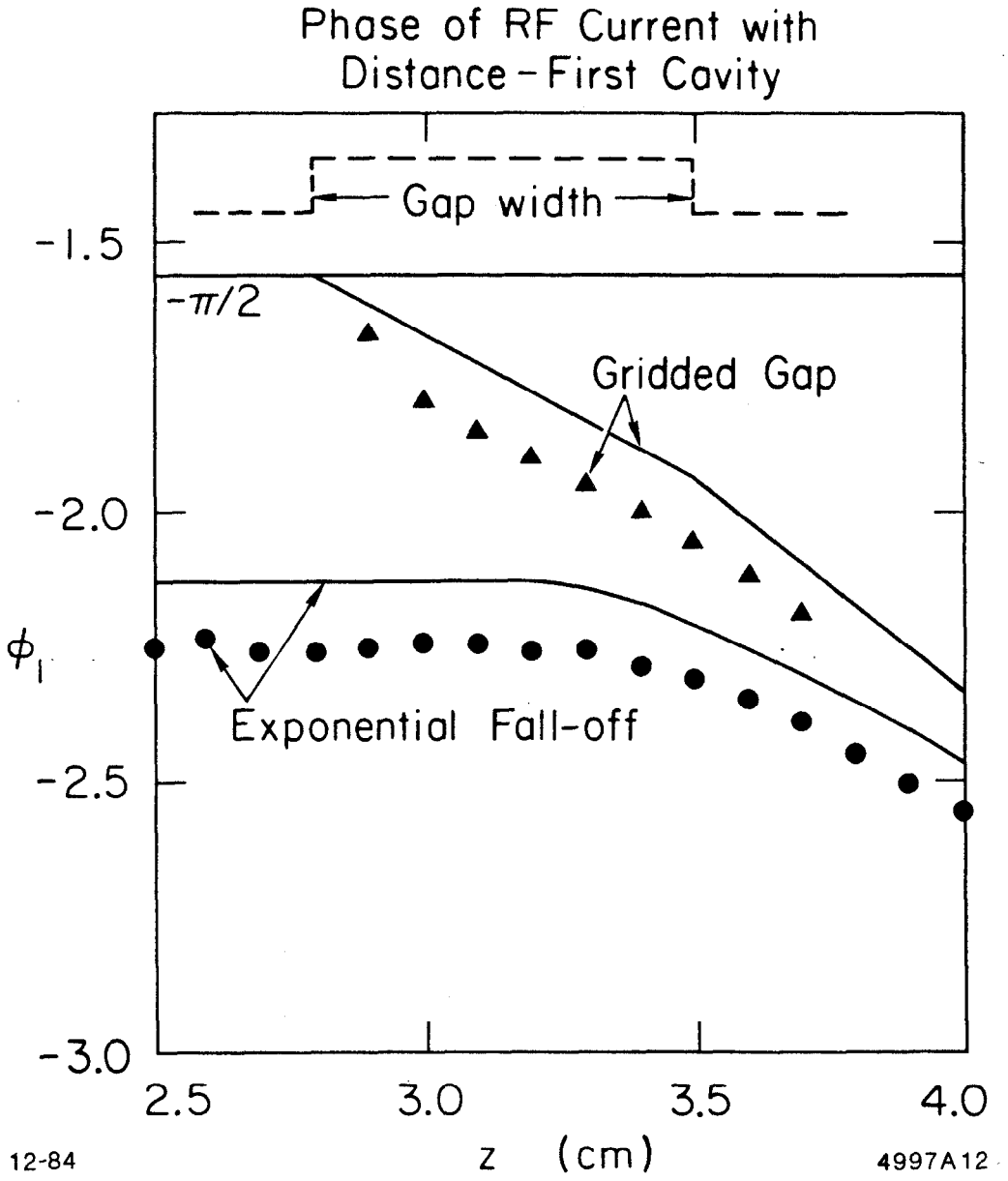
Phase of RF Current with
Distance - First Cavity
Gap width
-1.5
-π/2
Gridded Gap
-2.0
ϕ_1
Exponential Fall-off
-2.5
-3.0
2.5
3.0
3.5
4.0
12-84
z (cm)
4997A12

Fig. 12